


Assessment of the mixing-limited hypothesis with first-principles simulation results ^F

Cite as: Phys. Fluids **34**, 123328 (2022); <https://doi.org/10.1063/5.0126434>

Submitted: 15 September 2022 • Accepted: 02 December 2022 • Accepted Manuscript Online: 05 December 2022 • Published Online: 29 December 2022

 David P. Schmidt,  Marco Arienti,  José M García-Oliver, et al.

COLLECTIONS

 This paper was selected as Featured



View Online



Export Citation



CrossMark

ARTICLES YOU MAY BE INTERESTED IN

[Mesoscopic simulation of liquid bridge spreading under squeezing of parallel plates](#)

Physics of Fluids **34**, 123101 (2022); <https://doi.org/10.1063/5.0127420>

[Electric field enhancement of pool boiling of dielectric fluids on pillar-structured surfaces: A lattice Boltzmann study](#)

Physics of Fluids **34**, 123327 (2022); <https://doi.org/10.1063/5.0122145>

[Pore-scale modeling of multiphase flow in porous media using a conditional generative adversarial network \(cGAN\)](#)

Physics of Fluids **34**, 123325 (2022); <https://doi.org/10.1063/5.0133054>



Physics of Fluids

Special Topic: Food Physics

Submit Today!

Assessment of the mixing-limited hypothesis with first-principles simulation results

Cite as: Phys. Fluids **34**, 123328 (2022); doi: [10.1063/5.0126434](https://doi.org/10.1063/5.0126434)
Submitted: 15 September 2022 · Accepted: 2 December 2022 ·
Published Online: 29 December 2022



David P. Schmidt,^{1,a)}  Marco Arienti,²  José M García-Oliver,³  and José M. Pastor³ 

AFFILIATIONS

¹Department of Mechanical and Industrial Engineering, University of Massachusetts, Amherst, Massachusetts 01003, USA

²Thermal/Fluid Sciences and Engineering, Sandia National Laboratories, Mail Box 905 2, Livermore, California 94550, USA

³CMT-Motores Térmicos, Universitat Politècnica de València, 46022 Valencia, Spain

^{a)} Author to whom correspondence should be addressed: schmidt@umass.edu

ABSTRACT

Starting with two well-tested, one-dimensional models of non-evaporating, mixing-limited sprays, governing equations for liquid mass and two-phase momentum for each model can be manipulated to reveal the formal similarity between momentum and liquid volume fraction. The consequence of this similarity is that momentum, when properly non-dimensionalized, is equal to the liquid volume fraction at any time and at any axial location within a non-evaporating, mixing-limited spray with a constant rate of injection. An alternative, the more well-known similarity between mass fraction and velocity, is also mathematically evident. We compare predictions of this mathematical analysis to high-fidelity, first-principles simulation results of a non-evaporating spray to assess the validity of the theoretical similarity. The analysis of the simulation not only confirms the mathematical derivations but also points to subtlety in the definition of the spray velocity. In particular, the density-weighted velocity is required to observe similarity. The requirement of density-weighted velocity means that similarity tests require knowledge of both phase velocities. The agreement also works to confirm that the first-principles simulations are indeed mixing-limited, despite the finite nature of domain size and resolution.

Published under an exclusive license by AIP Publishing. <https://doi.org/10.1063/5.0126434>

I. INTRODUCTION

A crucial idea in spray research from the late 20th century was that the locally homogeneous flow (LHF) assumption could be used to model spray behavior. The main advocate of this theory, G. Faeth, explained that “The approximation requires that all phases have the same velocity and temperature, and that phase equilibrium is maintained at each point in the flow. Therefore, the use of an LHF model implies that the process is mixing controlled.”¹ Experimental data collected for evaporating sprays supported this model.

The realization that high-speed sprays could be mixing-limited fundamentally changed the understanding of sprays. The pivotal assumption of locally homogeneous flow is closely related to the assumption of mixing-limited flow. Siebers² found that spray evolution correlated with global parameters, such as spray angle, and that, under engine-relevant conditions, interfacial details played no observable role in spray evolution. Apparently, the interfacial area is so great that the mixing of ambient gas into the spray is the limiting factor in interfacial momentum and mass exchange. Consequently, spray evolution is dominated by turbulent mixing between the liquid and the ambient gas. In the absence of interfacial details, which

Siebers showed was not germane, the view of the spray was more of a continuum, such as would occur in the turbulent mixing of a high density gas jet.

Similar to these integral analyses, earlier work by Faeth¹ and Ruff *et al.*³ observed a parallel structure in the governing partial differential equations for transport of mixture fraction and momentum. Like the more recent works, the parallelism indicates similitude of velocity and mixture fraction. Neglecting pressure gradient, viscous energy dissipation, and assuming unity Lewis number and Schmidt number produces differential transport equations for mass, momentum, and energy that are identical once non-dimensionalized. The dimensionless boundary conditions are identical, leading to the existence of identical solutions among the governing equations.

This advance in our understanding of sprays led to a new class of one-dimensional, transient spray models that tended to have a set of common features and assumptions. The models extended the steady-state LHF models¹ to time-varying sprays with arbitrary rates of injection. These models were inspired by existing gas jet theories and assumed some shape of the radial profile.⁴ The models could then emphasize evolution of either centerline or transversely averaged

quantities. These models delivered fundamental insights into spray physics at a remarkably low cost.

One of the more useful models of transient, non-evaporating sprays was developed by Musculus and Kattke⁵ based on the principle of mixing-limited spray evolution.² This model includes the ability to capture transient effects and radial profiles in liquid volume fraction (LVF) and velocity. The validity of the model was checked against experimental data from subsequent studies by Musculus,⁶ Pickett *et al.*,⁷ Kook and Pickett,⁸ and Bardi *et al.*⁹ Often, the model is employed by fitting spray angle or coefficient of area of the nozzle, but the wide applicability and excellent agreement is still noteworthy.

Another relevant model is the one originally presented by Pastor *et al.*¹⁰ (hereafter, the DICOM model). This model is contemporary to the one by Musculus and Kattke, and it follows a very similar formulation as the discussion below will show. The performance of both models is similar, but DICOM has been extended under inert conditions to include real gas evaporation properties,¹¹ as well as heat release-derived changes in spray mixing behavior^{12,13} and even detailed chemistry effects that lead to ignition delay or lift-off length predictions.¹⁴

Since the evolution of these fundamental models, validated only against experimental data, the spray community has enjoyed the advent of highly resolved simulations based on first principles.^{15–19} These high-fidelity simulations offer the potential for assessing the assumptions of LHF and mixing-limited physics in a new way. While experiments offer the undeniable veracity of reality, the simulations offer a nearly unlimited ability to sample data that are experimentally inaccessible.

This article revisits the assumptions of both previous one-dimensional models for transient sprays using recently developed high-fidelity numerical results. We will study a canonical single-hole, plain orifice, spray. The focus of the present work is on non-evaporating conditions, for the sake of clarity. The present work will investigate the evidence of similitude between mass and momentum transfer and the evidence of mixing-limited behavior in the simulations. These kinds of similarities are a powerful tool for both modeling and experimental characterization of sprays, as demonstrated by the work of Buchmann *et al.*²⁰ The results will show new implications of the locally homogeneous flow modeling assumptions and reveal to what degree we may simplify the behavior of sprays to what amounts to a gas jet analogy.

The present work will extend a mathematical analysis of the one-dimensional models to show that the similarity is not limited to velocity and liquid mass fraction, as the past literature has emphasized.^{1,3,6} Manipulation of the equations show that another formal similarity exists between liquid volume fraction and momentum. In addition, the analysis shows both consistency and a few subtle differences between one-dimensional models. The fact that two different one-dimensional models yield the same similarity relationships indicates that the results of this paper are not tied to any one model.

The present work will examine the similarity relationships predicted by the one-dimensional models and then look for these similarities in high-fidelity CFD results, since finding them in experimental results is very difficult. These similarities, where present, can be used to predict one quantity from measurements of a different, similar, quantity.

II. ONE-DIMENSIONAL SPRAY MODELING

Our analysis begins with the governing equations used in 1D spray models. In general, a one-dimensional finite volume approach is

employed together with an *a priori* assumed radial profile for some of the transported variables, as illustrated in Fig. 1.

These 1D spray models make some general hypotheses that apply to any type of spray flow according to the following list:

1. Symmetry on the spray axis with no swirl.
2. Incompressible flow.
3. Turbulent (and molecular) viscous forces acting on each control volume are neglected. This assumption does not mean that turbulent effects are small, but that they disappear due to the type of control volume, which spans over the spray cross section until a radial position where gradients are very small.
4. Axial mixing due to molecular or turbulent diffusion is neglected, i.e., conservation equations only need to consider axial convection. This is a typical simplification used in boundary layer flows.²¹
5. Pressure gradients are neglected.
6. Radial profiles are defined for some of the transported variables. One of the variables is the axial component of the velocity vector, linked to the corresponding momentum equation. A second variable has to be linked to the fuel transport equation. In this case, liquid volume fraction is used by Musculus and Kattke,⁵ while mass fraction is used in DICOM.¹⁰ In DICOM, the mathematical formulation of these self-similar profiles remains constant along the whole calculation, even after the end of injection, while Musculus and Kattke use the evolving Abramovich²² gas jet profile.
7. Locally homogeneous flow, i.e., there exists a local equilibrium both in thermal and inertial conditions.

The two following additional hypotheses apply only for the type of spray flow of relevance for the present investigation, namely a non-evaporating spray:

1. For the present work, spray angle is constant during and after the end of injection. This results in a simple cone-shaped spray contour. This hypothesis has also been extended to a two-cone angle shape^{11,23} to get more accurate predictions of entrainment and hence penetration in the near-nozzle area.
2. There is no mass transfer between liquid and gas phase. This means that the phase separation is actually also a species separation, with the fuel species restricted to the liquid phase.

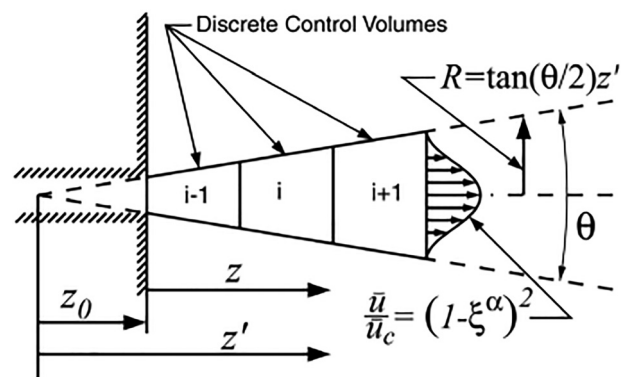


FIG. 1. Eulerian control volumes used in the Musculus–Kattke model. Taken from Musculus–Kattke.⁵

The starting point is a Reynolds-averaged approach for the differential conservation equations of fuel mass and momentum, followed by a Boussinesq-type approach with a turbulent viscosity to close the turbulent fluctuation terms. These equations are integrated over the particular cell to derive the corresponding integral equations, which according to the previous assumptions end up consisting of the time-derivative of the volume integral term and cell inlet and outlet convective flux terms. The conservation of liquid fuel mass, m_b , is given in Eq. (1) and the equation for axial momentum, M , is given in Eq. (2). Consistent with the non-vaporizing spray assumption, the momentum flux conservation is written for both phases as follows, although the fuel mass conservation equation is only for the liquid phase,

$$\frac{\partial m_l}{\partial t} = \dot{m}_{l,in} - \dot{m}_{l,out}, \tag{1}$$

$$\frac{\partial M}{\partial t} = \dot{M}_{in} - \dot{M}_{out}. \tag{2}$$

The unknown of the axial momentum equation is always the corresponding component of the convective velocity u . As for the fuel equation, at least two different options are available. Musculus and Kattke formulate their fuel conservation in terms of the liquid volume fraction X_l , consistent with an approach based on a multiphase flow description and similar to Siebers. The DICOM model, however, uses mixture fraction f as the unknown to be solved, which enables the later extension to reacting conditions. In principle, this could look like just a formulation detail, which should lead to the same solution with both variables being related by the following equation:

$$\rho_l X_l = \rho f. \tag{3}$$

Equation (3) reveals the non-linearity between X_l and f due to the ratio ρ_l/ρ . However, imposing a self-similar radial profile on either variable to convert the 2D problem into a 1D one produces some differences in results from both formulations in regions where there are important differences between liquid ρ_l and mixture density ρ .

Following the analysis of the conservation equations, both the liquid mass and momentum fluxes are defined using an integral across the cross section of the jet [Eqs. (4) and (5)]. Note that both phases are assumed to move at the same velocity and that all relevant magnitudes are Reynolds averaged:

$$\dot{m}_l = \int \rho_l X_l u dA = \int \rho f u dA, \tag{4}$$

$$\dot{M} = \int \rho u^2 dA. \tag{5}$$

Because the mixture density varies with location, it must remain within the integral of Eq. (5) or Eq. (4) in mixture fraction formulation. For a non-vaporizing spray, the mixture density is a simple function of both the fuel ρ_l and air density ρ_g , which is given as

$$\rho = \rho_l X_l + \rho_g (1 - X_l) = \frac{1}{\frac{f}{\rho_l} + \frac{1-f}{\rho_g}}. \tag{6}$$

At this point, another difference between formulations turns up when evaluating the integrals, and hence, impacts the solution obtained. While the DICOM model solves on-axis values for the

unknown quantities (f_{cl} , u_{cl}), i.e., values for radial coordinate $r=0$, Musculus and Kattke use cross-sectionally averaged values, which are denoted by an overbar (\bar{X}_l , \bar{u}) and follow the fundamental definitions given in the following equations:

$$\bar{X}_l = \frac{1}{A} \int X_l dA, \tag{7}$$

$$\bar{u} = \frac{1}{A} \int u dA. \tag{8}$$

Using either approach, the previous flux terms are re-written as shown in Eqs. (9) and (10), where additional terms appear, namely β in Musculus and Kattke, and P_u , P_f , and R in DICOM:

$$\dot{m}_l = \beta \rho_l \bar{X}_l \bar{u} A = f_{cl} u_{cl} A \int \rho P_u P_f d(r/R)^2, \tag{9}$$

$$\dot{M} = \beta \bar{\rho} \bar{u}^2 A = u_{cl}^2 A \int \rho P_u^2 d(r/R)^2. \tag{10}$$

The variable β is a varying quantity that describes the shape of the radial self-similar profile, R is the spray outer radius, as given by the cone angle, and is linked to the cross-sectional area A . P_u and P_f are the self-similar radial profiles for axial velocity and mixture fraction, respectively, which are assumed to follow a Gaussian distribution in the DICOM model according to Eqs. (11) and (12), where ζ is the value of the profile P_u defining the spray radial limit ($\zeta = 0.01$ in this work). Both distributions are related by the turbulent Schmidt number Sc :

$$P_u = \frac{u}{u_{cl}} = \exp[-\log(\zeta)(r/R)^2], \tag{11}$$

$$P_f = \frac{f}{f_{cl}} = P_u^{Sc}. \tag{12}$$

Further details on the formulations are given in the corresponding papers. For the present work, it is sufficient to know that β is a measure of correlation between the X_l and u profiles, as shown in following equation:

$$\beta = \frac{1}{\bar{X}_l \bar{u}} \int X_l u dA. \tag{13}$$

For a uniform radial profile, β is unity. For a fully developed profile, where the Abramovich²² radial profile is used, β is approximately 2. Though β represents a correlation between the two variables, X_l and u , the momentum flux depends on the square of velocity, requiring a correlation assessment of X_l and u^2 . However, Musculus and Kattke chose to use β in both calculation of mass and momentum flux for reasons of mathematical convenience.

A last difference in formulations between both models is related to the momentum equation. Musculus and Kattke made an assumption in Eq. (10) that density at a given radial cross section is constant and equal to the cross-sectional average density $\bar{\rho}$. Conversely, the DICOM model always operates with the local density definition, and conservation equations are solved by using numerical integration of the terms that account for local density.

III. MOMENTUM AND LIQUID TRANSPORT ANALOGY

Starting from the previously introduced equations of fuel mass and momentum, a theoretical analysis is included in the [Appendix](#)

showing that the transport equations for liquid volume fraction and non-dimensional momentum are identical and that the boundary conditions for both are identical, yielding the formal similarity stated in following equation:

$$\bar{X}_l = \bar{Q}. \tag{14}$$

The dimensionless momentum \bar{Q} represents the ratio of cross-sectionally averaged momentum divided by the momentum issuing from the nozzle, Eq (15). The value of $\bar{\rho}$, required in the definition of \bar{Q} , can be calculated from \bar{X}_l using Eq. (6). The fact that the numerator is $\bar{\rho}\bar{u}$ instead of $\overline{\rho u}$ is a consequence of the mathematical simplifications used in the one-dimensional models:

$$\bar{Q} \equiv \frac{\bar{\rho}\bar{u}}{\rho_l u_{inj}}. \tag{15}$$

Because the solution for liquid volume fraction must be unique, the end result is that dimensionless momentum equals liquid volume fraction at any time and axial location in non-evaporating, mixing-limited sprays. Measuring one of these quantities provides knowledge of the other. For example, if liquid volume fraction or velocity were available at a variety of transverse locations, one could use the fundamental definition of a cross-sectional average to calculate \bar{X}_l or \bar{u} [Eqs. (7) and (8)]. Though the value of u is strictly an average of the two phase velocities, the mixing-limited hypothesis assumes that the two phases are moving at the same velocity. This hypothesis opens the question, if only liquid or gas velocities were experimentally available, would these data be sufficient? This question will be answered later.

At first glance, this result may appear to be equivalent to that of Kastengren *et al.*²⁴ or Musculus.⁶ The difference is that the definition of momentum in the present work uses a density that is a weighted average of the gas and liquid density. Another subtle point of the present analysis is that if momentum and liquid volume fractions have the same transverse profile, then this result indicates that at every location, LVF and momentum ratio are equal, without any transverse integration. The present result applies to any part of the spray.

A manipulation of the governing equations shows that these prior results are in fact consistent with the present work. From Eq. (A13), we can substitute the elementary variables.

$$\frac{m_l}{\rho_l A \Delta z} = \frac{\bar{\rho}\bar{u}}{\rho_l u_{inj}}. \tag{16}$$

The liquid density cancels and the mixture density can be combined with the denominator of the left side to represent the total mass of all species (gas or liquid), hereafter m_t .

$$\frac{m_l}{m_t} = \bar{Y}_l = \frac{\bar{u}}{u_{inj}}. \tag{17}$$

Thus, when manipulated, the dimensionless velocity is proportional to mass fraction of liquid, as indicated by prior work. This proportionality is more apparent when one considers the DICOM model approach, where the fuel mass transport equation makes use of fuel mass fraction, resulting in an identical formulation to that of axial momentum. For a constant injection rate evolution, taking into account the boundary conditions, this can be shown to lead to the already known similarity between the solution of both variables for steady jets, as shown in classical gas-jet theory²⁵ and locally homogeneous flow analysis of sprays,¹

$$\frac{u}{u_{inj}} = f. \tag{18}$$

Combining the previous result with Eq. (3), one can obtain a similar relationship as in Eq. (14):

$$\frac{u}{u_{inj}} = \frac{\rho_l X_l}{\rho} \rightarrow X_l = \frac{\rho u}{\rho_l u_{inj}}. \tag{19}$$

Equations (19) and (18) turn out to be equivalent to Eqs. (14) and (17), as derived from the Musculus and Kattke model, but they are expressed in terms of local variables instead of cross-sectionally averaged ones.

IV. VERIFICATION AND VALIDATION

The first step in confirming the validity of this analysis is to verify the similarity against the predictions of the 1D models from which the present results are derived. This test serves as a check of the mathematical analysis.

The prediction of Eq. (14) is assessed in Fig. 2 for a high ambient pressure condition at an arbitrary time using a uniform rate of injection. The conditions are listed in Table I, and coincide with those later presented in the numerical simulation. This figure shows both \bar{Q} and \bar{X}_l plotted vs distance from the orifice using a line and symbols, respectively. Though the two models treat the leading edge slightly differently, in both cases, the results show that indeed, dimensionless momentum is equal to LVF in both 1D models. Thus, the derived results are not specific to any single 1D model. The next step is to determine if these model predictions correspond to more realistic representations of sprays.

Validation of the analysis was conducted using data generated by the CLSVOF CFD code applied to Spray D, as described in the study

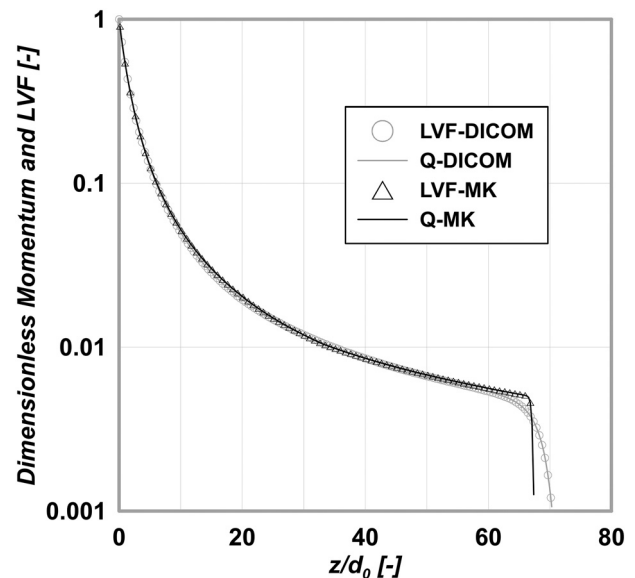


FIG. 2. Verification with DICOM and Musculus–Kattke model results. The dimensionless momentum and liquid volume fraction are plotted vs distance from the injector at a time of 0.05 ms after the start of injection. The leading edge of the spray is at 71d₀.

TABLE I. Parameters used in the CLSVOF Spray D simulation.

Parameter	Value
Liquid	n-Dodecane
Nozzle diameter	0.189 (mm)
Injection pressure	100 (MPa)
Fuel temperature	298 (K)
Gas density	22.8 (kg/m ³)
Ambient temperature	298 (K)

by Arienti and Sussman¹⁵ and applied in the work by Battistoni *et al.*²⁶ While, ideally, validation would involve experimental results, we have not been able to find sufficient data in the open literature. The experimental data would require both liquid volume and velocimetry measurements from the same regions of the spray without recourse to similarity assumptions as in the study by Kastengren *et al.*²⁴ Data would be required for the velocity of both phases under non-evaporating, mixing-limited conditions.

CLSVOF can provide high-fidelity, time-dependent datasets of spray velocity and mass distribution at injection conditions that are relevant to the mixing-limited hypothesis. The code numerically solves the compressible multi-phase Navier–Stokes equations in three dimensions while updating in time the interface separating the gas from the liquid phase. The main structure of the algorithm is described in a previous publication.²⁷ As evaporation is not included in the simulation, the interface effectively separates two immiscible fluids; surface tension is calculated from the local curvature. Spatial and temporal fluctuations of velocity in both phases are resolved to the degree allowed by grid resolution, with velocity continuity enforced at the interface; the subgrid turbulent fluctuations are modeled in the LES framework as added turbulent viscosity by following the WALE method.²⁸ Compressible effects are included;²⁷ the gas phase (modeled as a perfect gas) can become locally supersonic in diesel injections, and weak shocks have been observed at starting conditions.¹⁵ Naturally, the density of the liquid phase is not significantly affected by pressure variations at the conditions considered here.

Spray D is a single axial hole injector which, in this case, was discharged into high pressure, low temperature nitrogen. The conditions are summarized in Table I. Figure 3 shows a snapshot of the Spray D simulation, including the resolved liquid surface and the cross-sectional planes that will be discussed in this section. The surface tessellation used to represent the injector’s internal walls was obtained by combining x-ray computed tomography and optical microscopy images of the common-rail fuel injector Bosch 3–22 (specimen 209 134, or 134D). The exit diameter, calculated from the reconstructed orifice area, is $d_0 = 0.189$ mm, slightly smaller than the value reported by Payri *et al.*²⁹ for 134D of 0.191 mm.

The effective minimum grid resolution, obtained at the numerically reconstructed liquid surface by block-structured adaptive mesh refinement was $\Delta x = 3.5 \mu\text{m}$. This value is twice coarser than the Δx used in previous work²⁶ because here the simulation is designed to resolve the model-free dynamics of the liquid surface of the jet within a reasonable computational time, rather than the full range of droplet size distribution from primary atomization. The results are still time-accurate, and, as such, their analysis should be based on sample

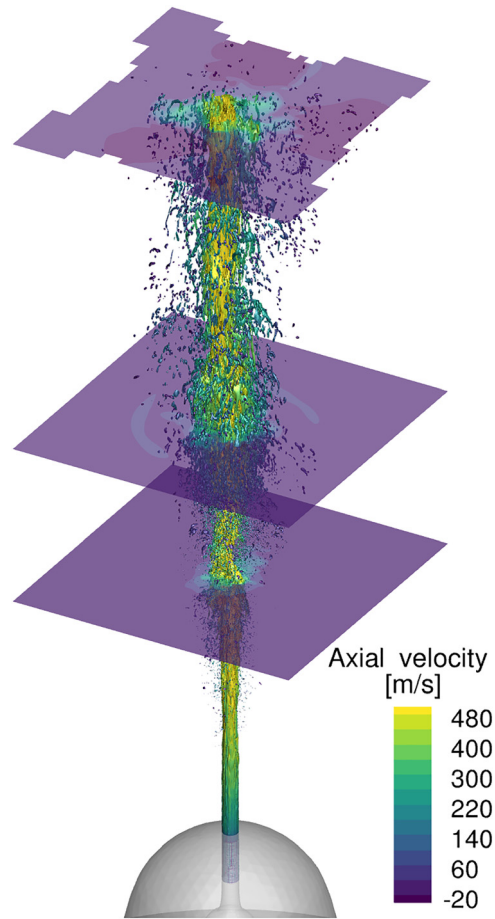


FIG. 3. Snapshot of CLSVOF Spray D simulation showing the resolved liquid surface and the cross-sectional planes used for analysis, all colored by axial velocity. The simulation includes the flow internal to the injector, which is partially visible in the picture.

averaging of multiple simulation instances at a given time. That approach, deemed too computationally demanding, is avoided here by replacing sample averaging with time averaging, at the price of restricting the scope of the validation to the steady-state portion of the jet.

Because the analysis in the current paper relies on a single uniform nozzle velocity u_{inj} , we must extract this value from the CFD results. Conceptually, our goal is to represent the nozzle exit profile with a reduced model as shown in Fig. 4. To do so, we follow the analysis of Payri *et al.*³⁰ In this model, the value of u_{inj} is presumed to be equal to an effective velocity u_{eff} issuing over an area A_{eff} that is less than the nozzle exit area. The values of u_{eff} and A_{eff} are calculated such that the effective area and velocity transit the same mass flow rate and momentum flux as the actual profile. These quantities are then employed in Eqs. (15) and (18).

To calculate u_{eff} from the CFD results, we use the following procedure. The value of u_{eff} is then used in the place of u_{inj} in the above analysis, particularly in Eqs. (18) and (17):

1. Calculate the Bernoulli velocity, u_{th} , from the upstream and downstream pressures

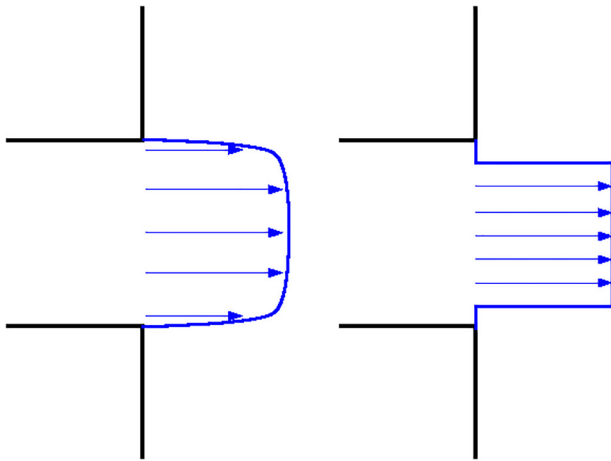


FIG. 4. Sketch of the exit velocity profile and the modeling assumptions used in the current paper. The three-dimensional exit profile (left) must be represented as a uniform profile with equivalent mass and momentum flux (right).

2. Calculate the average velocity, \bar{u} , based on mass flow rate from the nozzle
3. Calculate the coefficient of discharge C_d from \bar{u}
4. Calculate the value of the momentum coefficient C_M from the ratio of momentum flux and $2A\Delta P$
 $C_v = C_M/C_d$
5. The value of u_{eff} is $C_v u_{th}$

As in the rest of this section, integrals are calculated by numerical quadrature over the chosen cross section. From the conditions listed in Table I, and taking the reference value $\rho_l = 720 \text{ kg/s}$, we find $u_{th} = 522 \text{ m/s}$, whereas $\bar{u} = 497 \text{ m/s}$ from the time average of the simulation snapshots. Then, $C_M = 0.863$, $C_d = 0.915$, and $u_{eff} = 492 \text{ m/s}$. The range of velocity values reported by Payri *et al.*²⁹ at the same injection conditions (but with diesel instead of n-dodecane) is between 400 and 450 m/s.

Next, the cross-sectionally averaged values of X_l and \bar{u} are calculated from Eqs. (7) and (8). The application of the integral begs the question of the extent of the cross-sectional area. As the velocity profiles from the simulation tends to be wider than the LVF profiles, we consider two sets of data assuming 6° and 10° cone half angle. This discrepancy between the width of the LVF and the velocity profiles is explored in Sec. V.

The results of the comparison are shown in Figs. 5–8. They test the assertion that the cross-sectional averages (dashed lines) of Y and u are equal. The points in the diagram are temporal averages taken over the simulation samples (eight snapshots separated from each other by one microsecond) with error bands corresponding to their standard deviation. We observe that for both integration cone angles, the pairs (\bar{Y}, \bar{u}) are not close to equality. The discrepancy reflects the fact that velocity in the liquid phase is transferred to the gas phase more rapidly, or to a broader cross section, than the liquid mass, bound by surface tension; this delay is eventually recovered in the far field of the jet, as shown in Figs. 5 and 7. Depending on the cone angle, the presence of recirculating flow at the periphery of the jet (depending on the finite distance of the computational boundaries) may enter in the cross-sectional integral and further decrease \bar{u} .

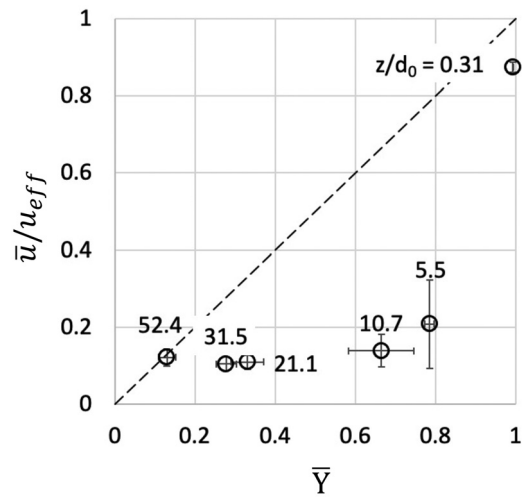


FIG. 5. Pairs of cross-sectional averages of mass fraction and axial velocity. The cone angle is 10° . The labels show the location of the cross sections. The error bars correspond to the standard deviation of the averages over the samples. The dashed line, $Y = X$, represents the theoretical equality of the two variables.

Examination of the mixing-limited assumptions reveals that both phases are supposed to be moving at the same velocity. Hence, one might conclude that the details of the velocity calculation are immaterial. However, per Ishii and Hibiki,³¹ the fluid center of mass moves with a density-weighted velocity. Their definition, however, requires time averaging of the quantities. In the current work, where data are extracted from three-dimensional snapshots, a cross-sectional averaging is used. Each cell in the CFD cross section is either fully liquid or gas, with the subscript k referring to the corresponding phase of that cell,

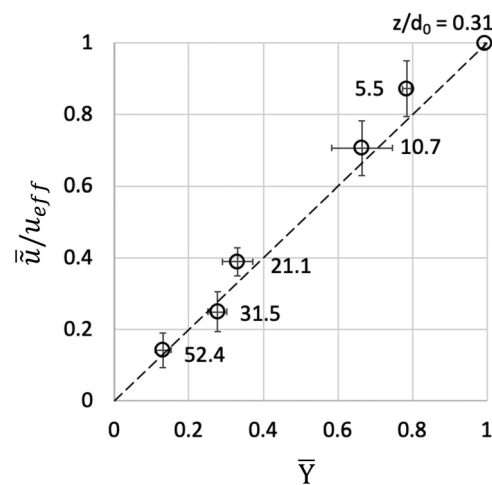


FIG. 6. Pairs of cross-sectional averages of mass fraction and density-weighted axial velocity. The cone angle is 10° . The labels show the location of the cross sections. The error bars correspond to the standard deviation of the averages over the samples. The dashed line, $Y = X$, represents the theoretical equality of the two variables.

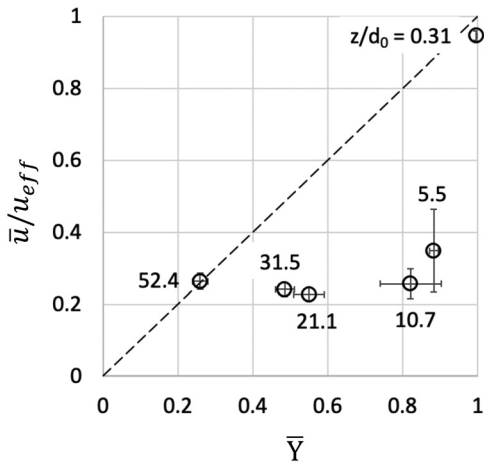


FIG. 7. Pairs of cross-sectional averages of mass fraction and axial velocity. The cone angle is 6°. The labels show the location of the cross sections. The error bars correspond to the standard deviation of the averages over the samples. The dashed line, $Y = X$, represents the theoretical equality of the two variables.

$$\bar{u} = \frac{\sum_A \rho_k u_k}{\sum_A \rho_k} \quad (20)$$

Because of the correlation between the distribution of velocity and liquid concentration, the mass-weighted average is significantly different than the unweighted average. Furthermore, the density-weighted velocity \bar{u} , which more closely corresponds to the velocity in the core of the jet, better approximates the cross-sectional average of the mass fraction as shown in Figs. 6 and 8. The observed similarities

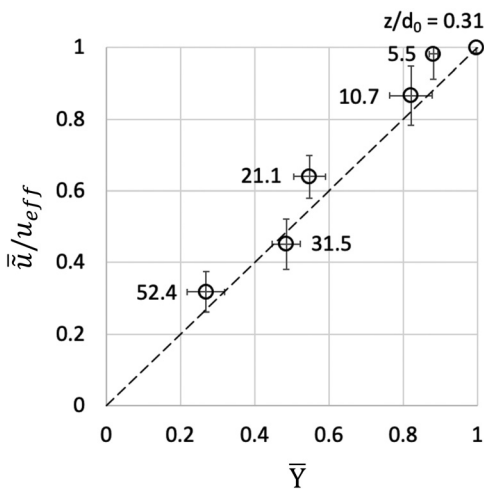


FIG. 8. Pairs of cross-sectional averages of mass fraction and density-weighted axial velocity. The cone angle is 6°. The labels show the location of the cross sections. The error bars correspond to the standard deviation of the averages over the samples. The dashed line, $Y = X$, represents the theoretical equality of the two variables.

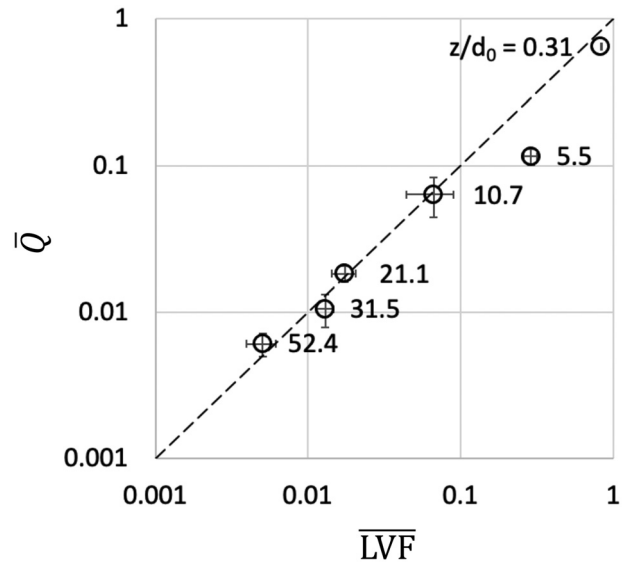


FIG. 9. Pairs of cross-sectional averages of liquid volume fraction and momentum. The cone angle is 10°. The labels show the location of the cross sections. The error bars correspond to the standard deviation of the averages over the samples. The dashed line, $Y = X$, represents the theoretical equality of the two variables.

are invariant of the assumed spray angle used for data collection. Analogously, Figs. 9 and 10 illustrate the model identity of cross-sectionally averaged liquid volume fraction and momentum for a cone angle of 10° and 6°, respectively (the $\bar{\rho u}$ integral is made non-dimensional by $\rho_l u_{eff}$). Again, while the numerical values depend on the assumed spray angle, for both spray angles, the pairs (\bar{LVF}, \bar{Q})

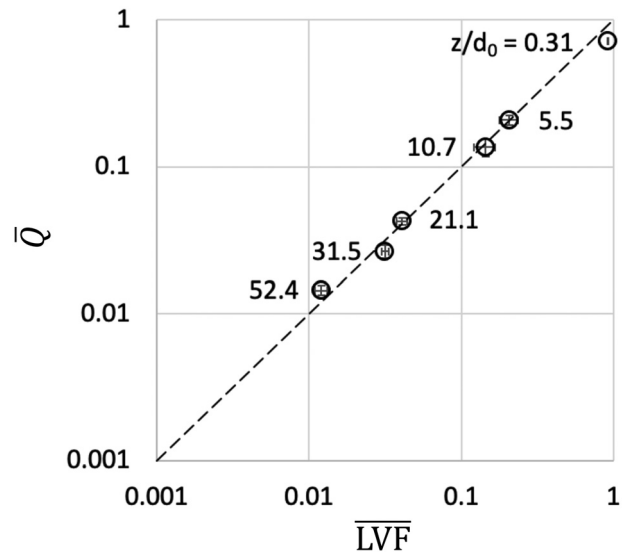


FIG. 10. Pairs of cross-sectional averages of liquid volume fraction and momentum. The cone angle is 6°. The labels show the location of the cross sections. The error bars correspond to the standard deviation of the averages over the samples. The dashed line, $Y = X$, represents the theoretical equality of the two variables.

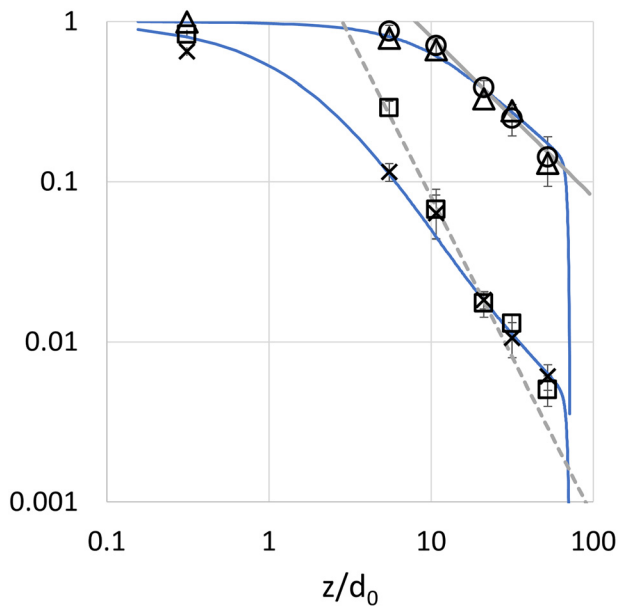


FIG. 11. Log–log plot of the cross-sectional averages of liquid mass fraction (circles), density-weighted axial velocity (triangles), liquid volume fraction (squares), and momentum (crosses) as a function of axial distance normalized by orifice diameter. The cone angle is 10° . The error bars correspond to the standard deviation of the averages over the samples. Blue lines are 1D model predictions corresponding to the cross-sectional averages of liquid mass fraction and liquid volume fraction at 0.05 ms. Gray dashed lines are used to show reference trends with $(z/d_0)^{-1}$ (solid) and $(z/d_0)^{-2}$ (dashed).

fall near the $Y = X$ line that represents the theoretical equality of the two variables. Another benefit of the density-weighted velocity is that the sensitivity to the assumed spray angle is minimal.

Plotted on log–log axes in Fig. 11, the pairs (\bar{Y}, \bar{u}) (circle and diamond symbols) follow the -1 slope suggested by round jet theory. The cross sections for $z < 10 d_0$ depart from that slope as \bar{Y} and \bar{u} decrease more slowly near the jet orifice. The cross-sectional averages of LVF and momentum (square and cross symbols) are similarly close, but they follow a steeper slope in the diagram, closer to -2 , due to the non-linear density effect. The 1D model predictions have also been included, showing a very good agreement with the simulation predictions in spite of the simplicity of the model approach. The comparison underlines the deviations of the CFD results in the near-injector field, caused by wall effects, from the fully self-similar behavior. Overall, our analysis highlights the fact that the 1D models exchange mass and momentum appropriately and can lead to a good estimation of major spray variables.

V. AN EXAMINATION OF RADIAL DISTRIBUTION

The distribution of LVF, axial velocity u , and fuel mass fraction Y_f are more closely examined in Fig. 12 at three cross sections located at 21.1, 31.5, and 52.4 d_0 from the nozzle exit. The first axial location is selected to probe the end of the jet core region, whereas the 52.4 d_0 cross section is taken almost at the end of the computational domain. The radial profiles are calculated as the time-average of eight snapshots separated from each other by one microsecond; they are plotted as a function of the radial distance from the geometrical axis of the jet,

normalized by r_0 . The velocity profiles are normalized by u_{th} and the momentum profiles by $\rho_l u_{th}$. Curves of the mean value plus or minus one standard deviation are added to the plots to convey the increasing fluctuation experienced by the jet downstream of the injection point. The curves show differences in noise levels connected to the discontinuous nature of density change in the primary atomization region and dense spray.³² The sharp density changes make the numerical convergence to an average value much slower compared to the velocity field, which must observe continuity in the gas-liquid interface. The more jagged features of some of the plots could therefore be explained in terms of requiring more snapshots for the analysis. Relevant to this point is the fact that the peak value of some of the profiles is not reached at the jet axis, suggesting that, further downstream, oscillations of the jet become sufficiently intense and of longer period that their dynamics are not completely captured within the averaging time window used here.

As expected, near the orifice, the radial profiles of the three variables are all smoothed-out approximations of the top-hat profile of Fig. 4. However, already at 20 orifice diameters from injection, the LVF profile remains visibly more compact than the velocity and mass fraction profiles. Further downstream, the radial profiles flatten to a more uniform distribution, but the spreading continues to occur at a greater rate for u and Y_f than for LVF. This feature is visible in pictures of the spray simulations, such as the one in Fig. 3, where the gas region that is entrained by the jet is much broader than the spray cone at every cross-sectional plane. This different behavior can be explained by considering that, while also promoting droplet pinch-off and breakup, surface tension tends to delay the diffusion of fuel mass. This effect impacts the distribution of liquid mass more than velocity and, therefore, affects the similarity of Y_f and velocity. So, the fact that similarity in mass fraction and velocity is observed in most of the jet confirms the low magnitude of surface tension effects and is consistent with the high Weber number associated with this spray.

Because of the large density ratio between liquid and gas, we can deduce that the normalized momentum of the flow and the liquid volume fraction of the jet eventually tend to follow a very similar radial profile, as concluded by our mathematical derivation. So, similarity is present, not just using cross-sectionally averaged quantities, but also in their radial distribution. Going even further in the analysis, these radial profiles are self-similar. The results of Fig. 13 show that by using the axial distance as a scaling factor for the radial distance, the curves at various axial distances collapse.

VI. CONCLUSIONS

Two different one-dimensional models have been compared to each other, both on a conceptual basis and using a practical example. These models give very similar results, and both indicate similarity relationships in the limit of mixing-limited spray behavior. Consequently, the analysis presented here is not a peculiarity of any single one-dimensional model. These similarities were sought in a high-fidelity CFD simulation of a non-evaporating spray.

The comparison to high-fidelity spray simulations begins to address the question of what similarity relationships are found in actual sprays. The results of the present work confirm that the high-fidelity simulations are able to capture these relationships, which do not depend on the assumed spray angle used for data extraction from the high-fidelity results. The more novel equivalence between liquid

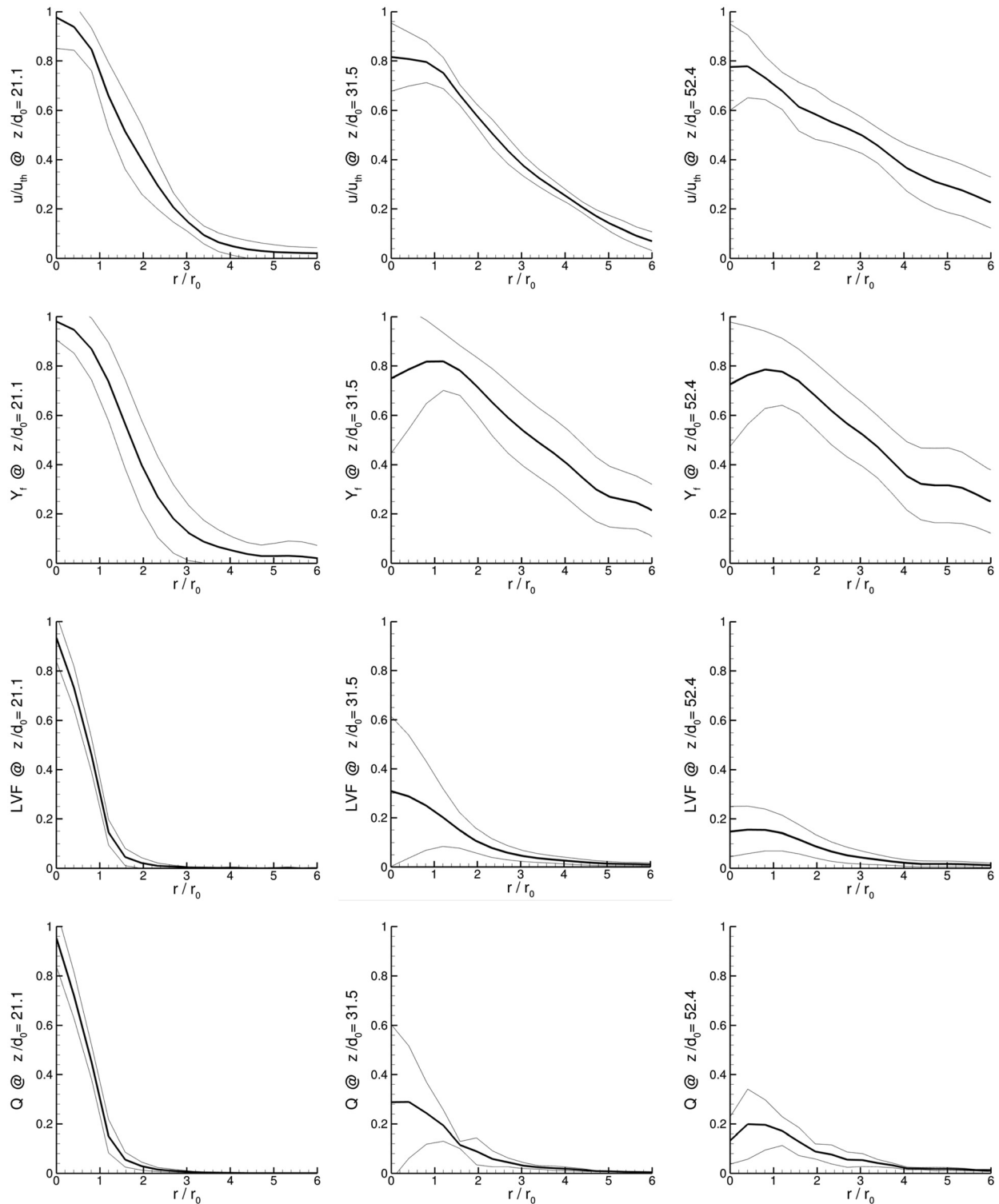


FIG. 12. Tangentially averaged profiles of axial velocity, liquid mass fraction, liquid volume fraction, and momentum (from top to bottom in the panel). The profiles are evaluated from the time-averaged CFD results at three axial locations: $21.1 d_0$, $31.5 d_0$, and $52.4 d_0$ from the nozzle exit; they are ordered from left to right in the panel. The thicker lines in each plot correspond to the average value from eight solution snapshots, the thinner lines represent the line average \pm one standard deviation.

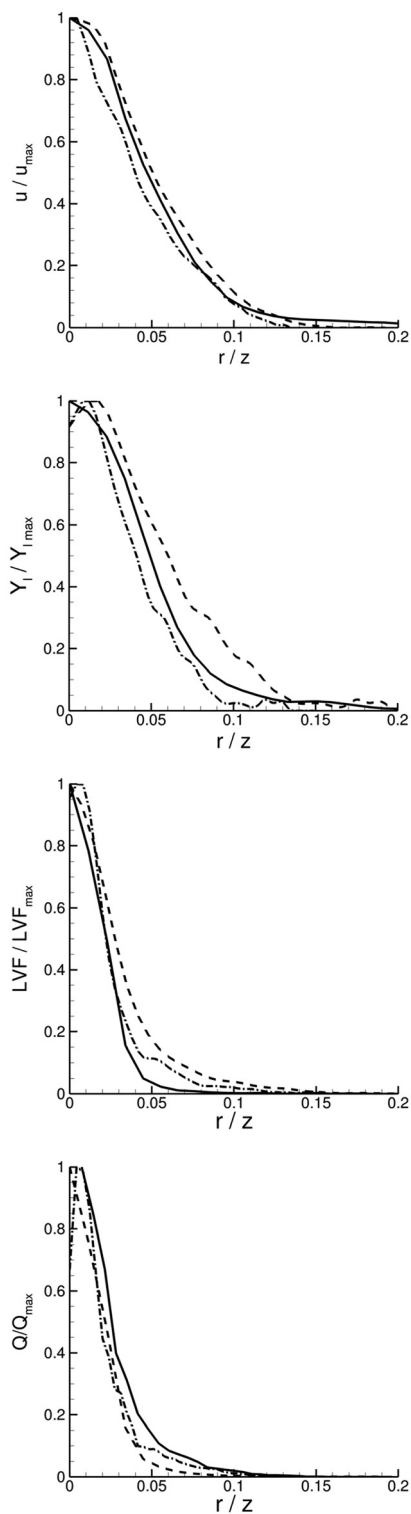


FIG. 13. Superimposed tangentially averaged profiles from Fig. 12. The radial length is scaled by the distance from the orifice, while the ordinate values are normalized using the maximum value of each profile.

volume fraction and momentum is evident in the results. Additionally, the similarity between velocity and mass fraction can be extracted from the CFD results, though doing so requires that the density-weighted velocity be used.

The reliance on a density-weighted velocity raises an interesting point for experimentalists. Typically, an experiment can measure the velocity of one phase or another, but not both phases. Thus, one would not expect experimentally measured velocity data to be sufficient for validating the velocity/mass fraction similarity seen in the simulation results. Though the density of the gas is much less than that of the liquid, at the elevated pressure conditions typical of mixing-limited sprays, the density of the gas phase is not negligible.

Evidence of similarity was more difficult to observe in tangentially averaged profiles. The effects of statistical noise were evident and the tendency of the spray to meander from the centerline made agreement with the similarity results more uncertain.

The observed decay and mixing rates deviated somewhat from round jet mixing theory. The exact reason for this deviation is unclear. It is, perhaps, an indication of the limitation of applying jet theory to two-phase mixing where the density ratio is large.

The agreement between the high-fidelity model and the one-dimensional models affirms the validity of the assumptions made in the construction of the one-dimensional models. In particular, the assumption of incompressibility is noteworthy, since the multi-dimensional calculations were compressible. At least for the metrics considered here, compressibility produces little observable effect, perhaps due to the absence of very strong pressure gradients in the free spray.

Given the high density ratio between phases, it may be unreasonable to expect that the unity Schmidt number assumption holds. Certainly, the transport of liquid mass into a region consisting of primarily of gas represents a shift of the center of mass that would not be observed in a uniform density gas jet. The shift in center of mass requires a force, such as a pressure gradient, that is not required for equal-density mixing and could break the similarity relationship. This difference between sprays and jets is significant because gas jets often serve as an inspiration for mixing-limited spray analyses. Further investigation should focus on the interplay between variable-density mixing and pressure gradients in sprays.

Taking the aforementioned results as a whole, we can make several specific and salient points. First, the similarity of momentum to liquid volume fraction is evident in the analysis of governing equations, one-dimensional models, and high-fidelity CFD. The similarity is not specific to any single one-dimensional model, but is rather a fundamental feature. Additionally, the fact that the CFD reproduces this particular behavior is evidence that the CFD is able to capture the mixing-limited behavior of ECN Spray D. Looking ahead, this similarity can be used in the construction of simplified models, as demonstrated by Buchmann *et al.*,²⁰ or to extend experiments where a measured quantity is used to estimate a formally similar quantity, as in Kastengren *et al.*²⁴ Perhaps, the theory could even be extended to flow-blurring spray regimes of more complex atomizers, as studied by Murugan *et al.*³³

ACKNOWLEDGMENTS

This study was supported by a grant from Sandia National Laboratories, a multi-mission laboratory managed and operated by

National Technology and Engineering Solutions for Sandia LLC, a wholly owned subsidiary of Honeywell International, Inc., for the U.S. Department of Energy's National Nuclear Security Administration under Contract No. DE-NA0003525.

AUTHOR DECLARATIONS

Conflict of Interest

The authors have no conflicts to disclose.

Author Contributions

David P Schmidt: Conceptualization (equal); Methodology (equal); Software (equal); Visualization (equal); Writing – original draft (equal); Writing – review & editing (equal). **Marco Arienti:** Conceptualization (equal); Methodology (equal); Writing – original draft (equal); Writing – review & editing (equal). **Jose M Garcia-Oliver:** Conceptualization (equal); Methodology (equal); Writing – original draft (equal); Writing – review & editing (equal). **Jose M. Pastor:** Conceptualization (equal); Methodology (equal); Writing – original draft (equal); Writing – review & editing (equal).

DATA AVAILABILITY

The data that support the findings of this study are available from the corresponding author upon reasonable request.

APPENDIX: DERIVATION OF THE ANALOGY BETWEEN MOMENTUM AND LIQUID TRANSPORT

The Musculus–Kattke model solves two transport equations using a control volume approach. In fact, for the case of constant injection velocity, the governing equations can be reformulated to show that there is a formal similarity between the liquid volume fraction and the two-phase momentum. The analysis begins with the Eqs. (1) and (2). The first step is to recast the transport of liquid mass into liquid mass fraction. This process begins by dividing the equation by $\rho_l A \Delta z \Delta t$:

$$\frac{m_{f,i}^{t+1} - m_{f,i}^t}{\rho_l A \Delta z \Delta t} = \frac{[(\beta \bar{X}_l \bar{u} A)_{i-1}^t - (\beta \bar{X}_l \bar{u} A)_i^t]}{A \Delta z} \tag{A1}$$

Note that ρ_l is a constant and $A \Delta z$ represents the finite volume. We use the definition of liquid volume fraction to replace m_l with \bar{X}_l :

$$\bar{X}_l = \frac{m_l}{\rho_l A \Delta z} \tag{A2}$$

Inserting this expression into Eq. (A1) and taking the limits as both Δz and Δt approach zero gives us a partial differential equation for the transport of \bar{X}_l :

$$\frac{\partial \bar{X}_l}{\partial t} = -\frac{\beta \bar{X}_l}{A} \frac{\partial}{\partial z} (\bar{u} A) \tag{A3}$$

The result in Eq. (A3) is sufficient for the present purposes, but for clarity of interpretation, the equation can be rearranged in a Lagrangian form. First, apply the product rule to the expression on the right:

$$\frac{\partial \bar{X}_l}{\partial t} = -\beta \bar{u} \frac{\partial \bar{X}_l}{\partial z} - \frac{\bar{X}_l}{A} \frac{\partial}{\partial z} (\beta \bar{u} A) \tag{A4}$$

Then, define a Lagrangian total derivative operator where the advection speed is defined as $\beta \bar{u}$. This appearance of β , which is greater than unity, shows that one consequence of the radial profile is to increase the average advection speed:

$$\frac{D(\)}{Dt} \equiv \frac{\partial(\)}{\partial t} + \beta \bar{u} \frac{\partial(\)}{\partial z} \tag{A5}$$

This operator can then be used to put Eq. (A4) into a Lagrangian form:

$$\frac{D \bar{X}_l}{Dt} = -\frac{\bar{X}_l}{A} \frac{\partial}{\partial z} (\beta \bar{u} A) \tag{A6}$$

An examination of this equation shows that it is linear. Thus, for a given $\beta(z)$, $\bar{u}(z)$ and $A(z)$, there exists only one solution for \bar{X}_l . In addition, the boundary conditions are unity at the injector orifice and zero in the limit of infinite z .

The next step is to perform an analogous manipulation of the momentum equation. This process begins by dividing the conservation of momentum equation [Eq. (A7)] by $A \Delta z \Delta t$:

$$M_i^{t+1} = M_i^t + [(\beta \bar{\rho} \bar{u}^2 A)_{i-1}^t - (\beta \bar{\rho} \bar{u}^2 A)_i^t] \Delta t, \tag{A7}$$

$$\frac{M_i^{t+1} - M_i^t}{A \Delta z \Delta t} = \frac{1}{A} \frac{[(\beta \bar{\rho} \bar{u}^2 A)_{i-1}^t - (\beta \bar{\rho} \bar{u}^2 A)_i^t]}{\Delta z} \tag{A8}$$

Momentum in the control volume is defined as follows:

$$M = \bar{\rho} \bar{u} A \Delta z \tag{A9}$$

Noting that A and Δz are not functions of time, the left side can be transformed into an expression for the time rate of change of $\bar{\rho} \bar{u}$. Using Eq. (A9) and taking the limits as Δt and Δz go to zero gives a partial differential equation for the transport of $\bar{\rho} \bar{u}$:

$$\frac{\partial \bar{\rho} \bar{u}}{\partial t} = -\frac{1}{A} \frac{\partial}{\partial z} (\beta \bar{\rho} \bar{u}^2 A) \tag{A10}$$

For steady injection conditions, the denominator of Eq. (15) is a constant and may be pulled into the temporal derivative. Whereas the density in the numerator is an average of the two phases, as defined by Eq. (6), the density in the denominator represents only the liquid density.

Inserting this expression into Eq. (A10) and scaling with $\rho_l u_{inj}$ gives a result that is analogous to the transport of mass, Eq. (A3) but in terms of the scaled momentum as defined in Eq. (A5):

$$\frac{\partial \bar{Q}}{\partial t} = -\frac{\bar{Q}}{A} \frac{\partial}{\partial z} (\beta \bar{Q} \bar{u} A) \tag{A11}$$

Applying the product rule and employing the same definition of Lagrangian derivative given in Eq. (A5) produces an expression for the evolution of momentum in the Lagrangian reference frame:

$$\frac{D \bar{Q}}{Dt} = -\frac{\bar{Q}}{A} \frac{\partial}{\partial z} (\beta \bar{u} A) \tag{A12}$$

Comparing Eqs. (A12) and (A6) reveals the formal similarity. Except for the symbol \bar{X}_l or \bar{Q} , these equations are identical. As for

\bar{X}_I , the boundary condition for \bar{Q} is unity at the injector and zero in the far field. Hence, these are the same equations and the same boundary conditions. We then apply the idea of mathematical similarity: if these are the same equations and boundary conditions, then they admit the same solution. Thus, the following equation is the ultimate result of this derivation:

$$\boxed{\bar{X}_I = \bar{Q}}. \quad (\text{A13})$$

REFERENCES

- ¹G. Faeth, "Evaporation and combustion of sprays," *Prog. Energy Combust. Sci.* **9**, 1–76 (1983).
- ²D. L. Siebers, "Scaling liquid-phase fuel penetration in diesel sprays based on mixing-limited vaporization," *SAE Trans.* **108**, 703–723 (1999).
- ³G. Ruff, A. Sagar, and G. Faeth, "Structure and mixing properties of pressure-atomized sprays," *AIAA J.* **27**, 901–908 (1989).
- ⁴N. Abani and R. D. Reitz, "Unsteady turbulent round jets and vortex motion," *Phys. Fluids* **19**, 125102 (2007).
- ⁵M. P. Musculus and K. Kattke, "Entrainment waves in diesel jets," *SAE Int. J. Engines* **2**, 1170–1193 (2009).
- ⁶M. P. Musculus, "Entrainment waves in decelerating transient turbulent jets," *J. Fluid Mech.* **638**, 117–140 (2009).
- ⁷L. M. Pickett, J. Manin, C. L. Genzale, D. L. Siebers, M. P. Musculus, and C. A. Idicheria, "Relationship between diesel fuel spray vapor penetration/dispersion and local fuel mixture fraction," *SAE Int. J. Engines* **4**, 764–799 (2011).
- ⁸S. Kook and L. M. Pickett, "Liquid length and vapor penetration of conventional, Fischer–Tropsch, coal-derived, and surrogate fuel sprays at high-temperature and high-pressure ambient conditions," *Fuel* **93**, 539–548 (2012).
- ⁹M. Bardi, R. Payri, L. M. C. Malbec, G. Bruneaux, L. M. Pickett, J. Manin, T. Bazyn, and C. L. Genzale, "Engine combustion network: Comparison of spray development, vaporization, and combustion in different combustion vessels," *Atomization Sprays* **22**, 807 (2012).
- ¹⁰J. V. Pastor, J. J. López, J. M. García, and J. M. Pastor, "A 1D model for the description of mixing-controlled inert diesel sprays," *Fuel* **87**, 2871–2885 (2008).
- ¹¹J. V. Pastor, J. M. Garcia-Oliver, J. M. Pastor, and W. Vera-Tudela, "One-dimensional diesel spray modeling of multicomponent fuels," *Atomization Sprays* **25**, 485–517 (2015).
- ¹²J. M. Desantes, J. J. Lopez, J. M. Garcia, and J. M. Pastor, "Evaporative diesel spray modeling," *Atomization Sprays* **17**, 193 (2007).
- ¹³J. M. Garcia-Oliver, L. M. Malbec, H. B. Toda, and G. Bruneaux, "A study on the interaction between local flow and flame structure for mixing-controlled diesel sprays," *Combust. Flame* **179**, 157–171 (2017).
- ¹⁴J. M. Garcia-Oliver, R. Novella, J. M. Pastor, L. Pachano, and B. Naud, "A quasi-1D model for the description of ECN spray a combustion process," in SAE Technical Paper No. 2020-01-0661, 2020.
- ¹⁵M. Arienti and M. Sussman, "A numerical study of the thermal transient in high-pressure diesel injection," *Int. J. Multiphase Flow* **88**, 205–221 (2017).
- ¹⁶M. Herrmann, "A parallel Eulerian interface tracking/Lagrangian point particle multi-scale coupling procedure," *J. Comput. Phys.* **229**, 745–759 (2010).
- ¹⁷S. S. Deshpande, S. R. Gurjar, and M. F. Trujillo, "A computational study of an atomizing liquid sheet," *Phys. Fluids* **27**, 082108 (2015).
- ¹⁸R. Lebas, T. Menard, P.-A. Beau, A. Berlemont, and F.-X. Demoulin, "Numerical simulation of primary break-up and atomization: DNS and modeling study," *Int. J. Multiphase Flow* **35**, 247–260 (2009).
- ¹⁹B. Wang, M. Cleary, and A. Masri, "Modeling of interfacial flows based on an explicit volume diffusion concept," *Phys. Fluids* **33**, 062111 (2021).
- ²⁰N. A. Buchmann, D. J. Duke, S. A. Shakiba, D. M. Mitchell, P. J. Stewart, D. Traini, P. M. Young, D. A. Lewis, J. Soria, and D. Honnery, "A novel high-speed imaging technique to predict the macroscopic spray characteristics of solution based pressurised metered dose inhalers," *Pharm. Res.* **31**, 2963–2974 (2014).
- ²¹H. Schlichting and K. Gersten, *Boundary-Layer theory*, Ninth ed. (Springer, Berlin, Heidelberg, 2017).
- ²²G. N. Abramovich, *The Theory of Turbulent Jets* (The MIT Press, 1963).
- ²³L. M. Pickett, J. Manin, R. Payri, M. Bardi, and J. Gimeno, "Transient rate of injection effects on spray development," SAE Technical Paper No. 2013-24-0001, 2013.
- ²⁴A. L. Kastengren, C. F. Powell, S.-K. Cheong, Y. Wang, K.-S. Im, X. Liu, J. Wang, and T. Riedel, "Determination of diesel spray axial velocity using x-ray radiography," in SAE Technical Paper No. 2007-01-0666, 2007.
- ²⁵D. B. Spalding, *Combustion and Mass Transfer—A Textbook with Multiple-Choice Exercises for Engineering Students* (Pergamon, 1979).
- ²⁶M. Battistoni, G. M. Magnotti, C. L. Genzale, M. Arienti, K. E. Matusik, D. J. Duke, J. Giraldo, J. Ilavsky, A. L. Kastengren, C. F. Powell *et al.*, "Experimental and computational investigation of subcritical near-nozzle spray structure and primary atomization in the engine combustion network spray D," *SAE Int. J. Fuels Lubr.* **11**, 337–352 (2018).
- ²⁷M. Jemison, M. Sussman, and M. Arienti, "Compressible, multiphase semi-implicit method with moment of fluid interface representation," *J. Comput. Phys.* **279**, 182–217 (2014).
- ²⁸F. Nicoud and F. Ducros, "Subgrid-scale stress modelling based square velocity gradient tensor," *Flow, Turbul. Combust.* **62**, 183–200 (1999).
- ²⁹R. Payri, J. Gimeno, J. Cuisano, and J. Arco, "Hydraulic characterization of diesel engine single-hole injectors," *Fuel* **180**, 357–366 (2016).
- ³⁰R. Payri, J. Garcia, F. Salvador, and J. Gimeno, "Using spray momentum flux measurements to understand the influence of diesel nozzle geometry on spray characteristics," *Fuel* **84**, 551–561 (2005).
- ³¹M. Ishii and T. Hibiki, *Thermo-Fluid Dynamics of Two-Phase Flow* (Springer Science & Business Media, 2010).
- ³²F. Abbas, B. Wang, M. Cleary, and A. Masri, "Numerical convergence of volume of fluid based large eddy simulations of atomizing sprays," *Phys. Fluids* **33**, 042119 (2021).
- ³³R. Murugan, P. S. Kolhe, and K. C. Sahu, "A combined experimental and computational study of flow-blurring atomization in a twin-fluid atomizer," *Eur. J. Mech.-B/Fluids* **84**, 528–541 (2020).